Local stress and strain in heterogeneously deformed aluminum: a comparison analysis by microhardness, electron microscopy and finite element modelling

Zhang, Xiaodan; Nielsen, Chris V.; Hansen, Niels; Silva, Carlos M.A.; Martins, Paulo A. F.

Published in:
International Journal of Plasticity

Link to article, DOI:
10.1016/j.ijplas.2018.11.014

Publication date:
2019

Document Version
Peer reviewed version

Accepted Manuscript

Local stress and strain in heterogeneously deformed aluminum: a comparison analysis by microhardness, electron microscopy and finite element modelling

Xiaodan Zhang, Chris V. Nielsen, Niels Hansen, Carlos M.A. Silva, Paulo A.F. Martins

PII: S0749-6419(18)30469-8

DOI: https://doi.org/10.1016/j.ijplas.2018.11.014

Reference: INTPLA 2449

To appear in: *International Journal of Plasticity*

Received Date: 23 July 2018

Revised Date: 22 November 2018

Accepted Date: 22 November 2018

Please cite this article as: Zhang, X., Nielsen, C.V., Hansen, N., Silva, C.M.A., Martins, P.A.F., Local stress and strain in heterogeneously deformed aluminum: a comparison analysis by microhardness, electron microscopy and finite element modelling, *International Journal of Plasticity*, https://doi.org/10.1016/j.ijplas.2018.11.014.

Local stress and strain in heterogeneously deformed aluminum: a comparison analysis by microhardness, electron microscopy and finite element modelling

Xiaodan Zhang[1], Chris V. Nielsen[1], Niels Hansen[2], Carlos M. A. Silva[3], Paulo A. F. Martins[3]

[1]Department of Mechanical Engineering, Technical University of Denmark, 2800 Kgs. Lyngby, Denmark
[2]Department of Wind Energy, Technical University of Denmark, Risø campus, DK-4000, Roskilde, Denmark
[3]IDMEC, Instituto Superior Técnico, Universidade de Lisboa, Av. Rovisco Pais, 1049-001 Lisboa, Portugal

Abstract

The local stress and strain are analysed in a heterogeneous microstructure induced by compression of aluminium rings under nearly full sticking conditions. This analysis is based on characterization of mechanical behaviour and microstructure applying three complementary techniques covering multiple length scales: microhardness, electron microscopy (electron backscatter diffraction) and finite element modelling. The findings are underpinned by applying those techniques in an analysis of a homogeneous microstructure induced by compression of hot-extruded aluminium cylinders. The local stress and strain are estimated at 14 different positions in two rings representing large variations in strain. A comparison with the stress and strain in the homogeneously compressed cylinders related to the average spacing between deformation induced low and high angle boundaries, validates the characterization techniques and supports a hypothesis that the microstructure of local regions in a heterogeneous structure evolve in accordance with universal principles and mechanisms established for the evolution of the deformation microstructure of polycrystalline metals.

Keywords: heterogeneous structure; aluminium; microstructure; microhardness; electron microscopy; finite element modelling; compression; ring tests.

1. Introduction

Metals and alloys undergoing thermo-mechanical plastic deformation are typically investigated on the assumption that the process and the resultant microstructure are homogeneous. This has led

to formulation of universal principles and mechanisms for the evolution of the deformation microstructure of polycrystalline metals (Hughes and Hansen, 2004). However, the evolution of stress and strain during plastic deformation may not be homogeneous, for example, in a forming operation where friction and wear are important part of the process. A heterogeneous structure may also be induced deliberately, for example by plastic deformation of a surface to increase wear and fatigue resistance of a component.

Investigation of the mechanical behavior of heterogeneously deformed metals requires a methodology that accounts for variations of structural parameters and strength on multiple length scales from the sub-micrometer dimension to the macroscopic scale. In the present study authors characterize a heterogeneous structure in aluminum and use three complementary characterization techniques: (i) microhardness, (ii) electron microscopy and (iii) finite element modelling (FEM). It is the intention of this work to characterize the local stress and strain in a heterogeneous structure which is induced by compression of aluminum rings under nearly full sticking conditions. The local stress and strain will be characterized by the three techniques which will be validated through a comparative analysis.

The quantification of local stress and strain in the compressed rings will be based on the average spacing between low angle boundaries (LABs) and high angle boundaries (HABs) and the relationship between this parameter and the stress and strain, respectively. These relationships are formulated based on the characterization of homogeneously compressed aluminum cylinders to obtain corresponding values of stress, strain and boundary spacing. This methodology is based on the hypothesis that the characteristics of local regions in a heterogeneous structure may evolve in accordance with universal principles and mechanisms obtained for the evolution of the deformation microstructure of polycrystalline metals.

2. Experimental

A hot extruded AA 1050 $\varnothing 25mm$ round bar with the chemical composition Al-0.056Si-0.17Fe-0.002Mn-0.006Ni-0.006Zn-0.005Ti-0.003Zr-0.007V (wt. %) was utilized for homogeneously compressed cylinders and heterogeneously compressed rings.

Microstructural characterization has been carried out on the cross-section of the cylinders and rings (see Fig. 1 for rings and Fig. 3 for cylinders). For rings, the classification of three zones (outer side, sticking and inner side zones) is based on the colour contrast on the top plane of the ring, as shown in Fig. 1b, where the dark grey middle zone represents the original surface before compression and the grey zones on each side represent new surfaces formed during compression. The samples for microstructural characterization in a scanning electron microscope (SEM) are cut from cylinders and rings (Fig. 3a and Fig. 1b), ground with water-proof sand papers from 300#, 1000# to 4000#, mechanically polished with 40nm Al_2O_3 suspension, electro-polished with the A2 polishing solution typically for aluminium and aluminium alloys. Backscatter imaging and electron backscatter diffraction (EBSD) have been applied to quantify the microstructure, crystallographic orientation and (micro) texture (Zhang, 2009; Zhang et al., 2011; Fan et al., 2014; Zhang et al., 2018). The step sizes for EBSD scanning are 1000nm, 200nm and 120nm according to the fineness of the deformation structure. The finer the deformation structure, the smaller the chosen step size. TEM foils are made via a double-jet electro polishing technique applied in recent studies (Zhang et al., 2012b; Chen et al., 2015; Zhu et al., 2017; Nikas et al., 2018). The TEM foils are investigated using a JEOL 2000FX TEM at 200 kV. The microhardness (Vickers, $HV_{0.01}$ and $HV_{0.05}$) profiles are measured using a Struers Durascan microindentor with a load of 10g and 50g where $HV_{0.05}$ is only used in Section 3.2 to check the microhardness homogeneity of compressed cylinders and $HV_{0.01}$ is used in all the rest of the paper. It should be noted that the $HV_{0.01}$ and $HV_{0.05}$ values are consistent with each other and that diagonals of indents under both loads are larger than 20 μm.

The applied techniques are complementary and have different spatial resolution. This study applies different techniques for microstructural and mechanical characterization: electron

microscopy (EBSD, SEM and TEM), FEM and microhardness. The spatial resolution and the applied scale of these techniques are listed in Table 1. The scale, for EBSD is the square area side length, for SEM and TEM the small and large observation area side length, for FEM the scale represents the mesh size, and for microhardness it is the indent diagonal. This diagonal is obtained from the area characterized by EBSD. The applied scales for the different techniques are of the same order to produce comparable average data for analysis.

Table 1. Average values of the microstructural parameters as a function of strain for AA 1200

Techniques	Spatial resolution	Applied scale
EBSD	5 ~ 10 nm	20 ~ 80 μm
SEM	~ 1 nm	20 ~ 600 μm
TEM	< 1 nm	20 ~ 200 μm
FEM	-	~ 50 μm
Microindentation	Down to several micrometres	20 ~ 30 μm

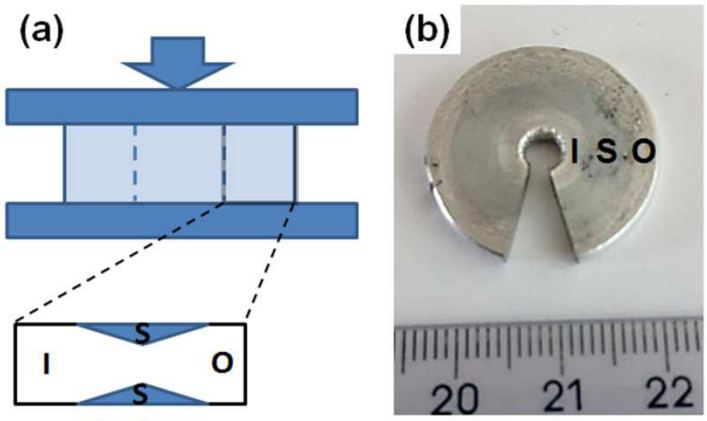

Figure 1. (a) Sketch showing the ring compression and sample-taking for microstructural characterization and hardness; (b) real sample showing the outer side (O), sticking (S) and inner side (I) zones.

Fig. 2 shows the initial microstructure in the hot-extruded AA 1050 bar. The bar has a <100> extrusion texture typical for pure Al. The mixture of large (~ 200 μm) and small (~ 5 μm) grains gives an average grain size around 47 μm. The dislocation structure comprises single dislocations and dislocation tangles in the grains (Fig. 2b). The dislocation density measured by the intersection method is about 1×10^{13} m^{-2}. Particles ranging from 200 nm to ~ 2 μm shown in Fig. 2d are intermetallic AlFeSi and AlFeSiMn particles from the original bar, of AA 1050 (Belov et al., 2002). Based on the morphology as shown in Fig. 2a and 2e, a matrix for the microhardness tests has been chosen (Fig. 2f) showing the position of 20 indents over an area of 800 × 300 μm^2. It is found that

the hardness is homogeneous in the hot extruded bar with an average value of 28.3 kgf/mm^2 with a standard deviation 0.8 kgf/mm^2.

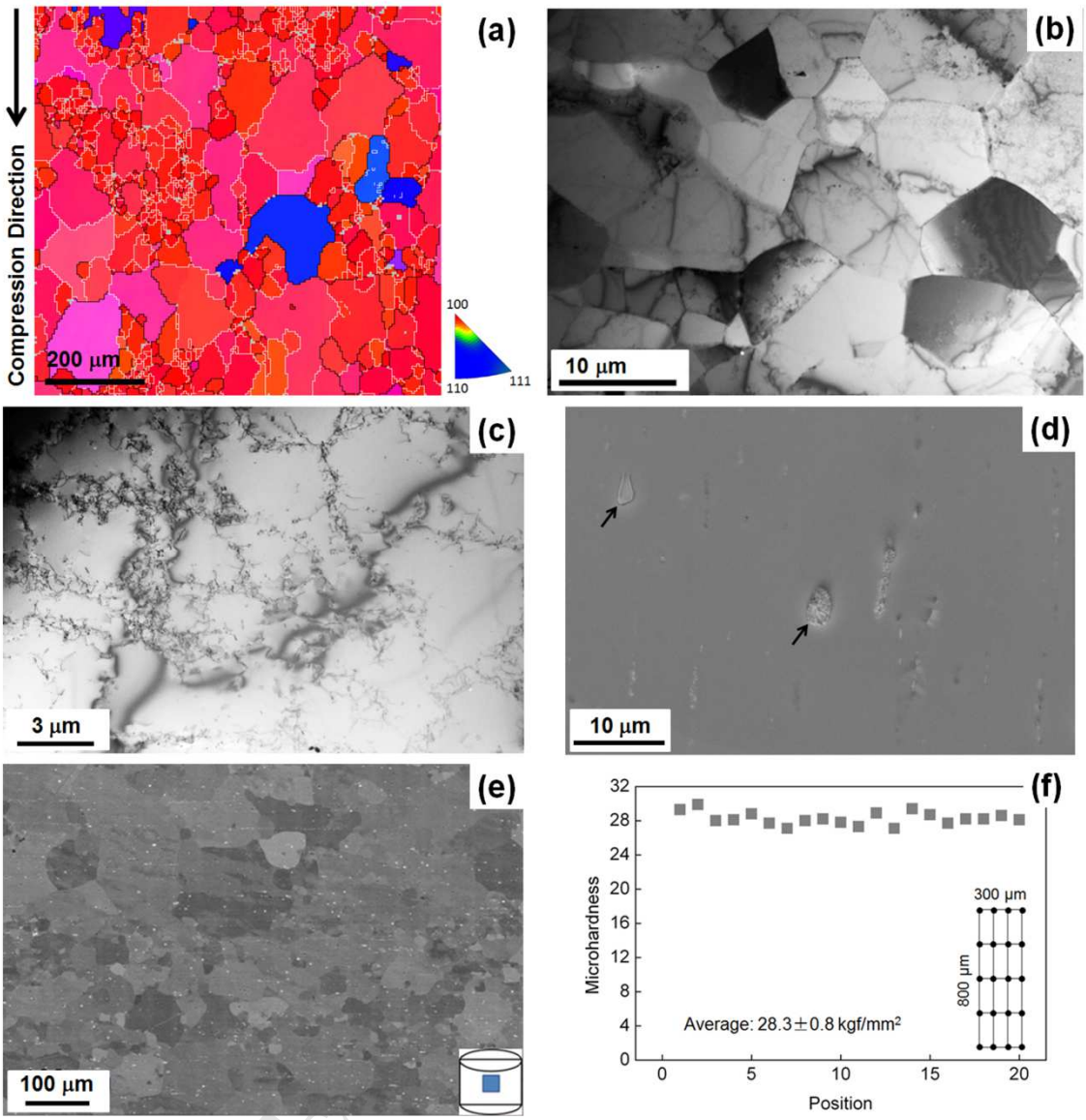

Figure 2. Initial microstructure of AA 1050. (a) electron backscatter diffraction (EBSD) micrograph; (b) transmission electron microscopy (TEM) micrograph showing a small grain structure in (a); (c) TEM micrograph showing dislocation tangles in a grain; (d) intermetallic particles in a matrix of AA 1050 with micrometer-sized particles indicated by black arrows; (e) SEM backscattered micrograph showing a similar microstructure as shown by EBSD and intermetallic particles marked as white dots; (f) the hardness based on 20 indents where the numbers 200 µm and 100 µm represent the distance between neighboring rows and columns (see text).

3. Homogeneous deformation of cylinders

3.1 Compression tests of cylinders

The analysis of the homogeneously compressed cylinders has two objectives: (i) to obtain values of hardness and flow stress as a function of strain and (ii) to obtain relationships between structural

parameters and flow stress and strain. The test matrix is shown in Table 2. It is found that the compression to a strain beyond 1 will transform the cylinder samples to a drum shape. For further compression to higher strains, test specimens have been machined from a pre-compressed cylinder to accumulate strain, (see Table 2 and Fig. 3).

Table 2. Homogeneously compressed cylinders

Strain	Sample dimension	
	Height (mm)	Diameter (mm)
0	18	18
0.31	13.2	21.0
0.70	8.9	25.6
0.96	6.9	29.1
0	22.5	22.0
1.00	8.1	36.7
1 (machined for further compression)	8.0	8.0
1.44	5.2	9.9
1.90	3.4	12.4

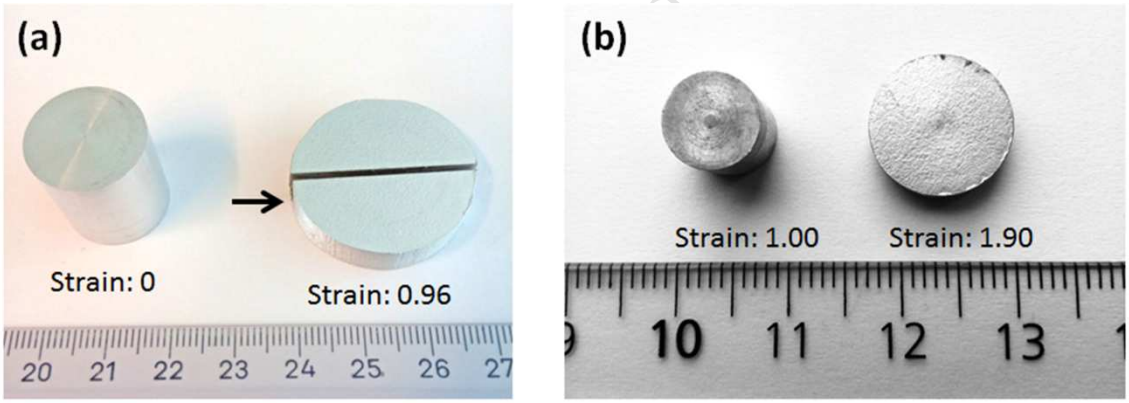

Figure 3. Shapes and dimensions of homogeneously compressed cylinders to different strains (see Table 1). The black area points to the section for hardness testing and microstructural characterization. The hardness measurements are shown in Fig. 4 illustrating a relatively small variation demonstrating structural homogeneity.

3.2 Microhardness homogeneity of compressed cylinders

Vickers microhardness $HV_{0.05}$ was performed across the radius of a cylinder, as shown for a sample at a strain of 1 (Fig. 4). Results show that the center part is slightly harder than the edges. However, taken into account that the error is around 3 due to inclusions in Al (as will be clear later in relation to Fig. 2), this distribution can, with a good approximation, be considered homogeneous with a difference between the highest and lowest hardness of 3. An area around at a position at half radius (within the white frame in Fig. 4) has therefore been selected as the area for further testing.

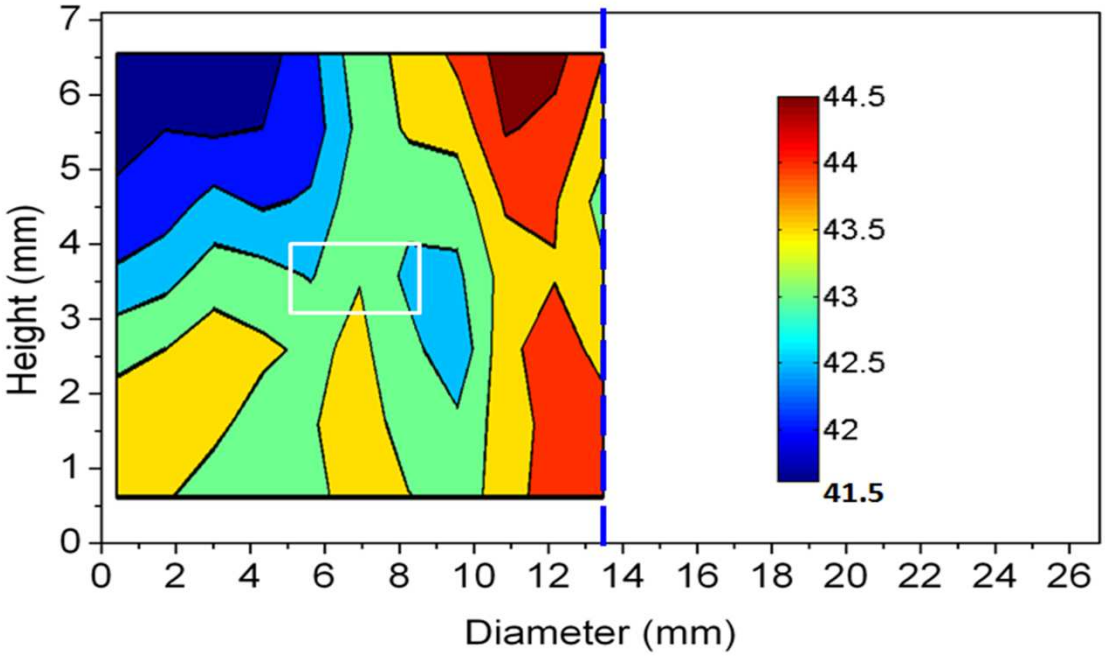

Figure 4. Hardness distribution in the cross section of the homogeneously compressed cylinder at a strain of 1. The dashed line represents the middle line. The thin black frame shows the border of the electro-polished sample. In the colored column the hardness $HV_{0.05}$ varies from 41.5 to 44.5.

3.3 Compression of cylinders: stress-strain relationship

The flow stress of the original and pre-strained (a strain of 1) cylinders are determined by uniaxial compression testing. The combined curve (see Fig. 5) is fitted by a Hollomon expression extrapolated to a strain of 2.5,

$$\bar{\sigma} = 126\bar{\varepsilon}^{0.23} \tag{1}$$

which is used in the numerical simulations of the rings made of the original bar material. For simulations of the rings made from pre-strained material, a Swift equation is applied,

$$\bar{\sigma} = 126\left(1+\bar{\varepsilon}\right)^{0.23} \tag{2}$$

which corresponds to simulation based on Equation (1) but starting with a pre-strain $\bar{\varepsilon} = 1.00$.

The stress-strain curve in Fig. 5 shows the typical hardening behavior in 2 stages. Parabolic hardening at small and medium strains with decreasing hardening rate (stage III) and almost linear hardening at large strain have been observed (stage IV).

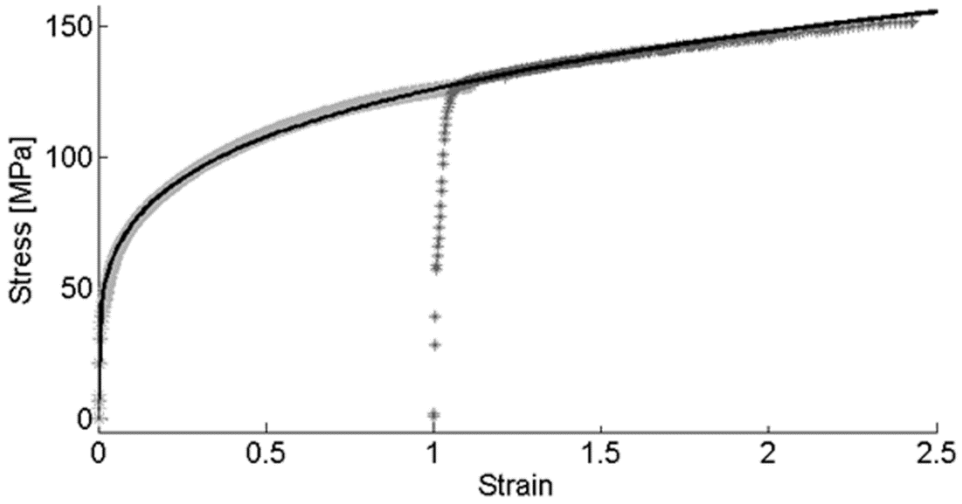

Figure 5. Combined flow stress curve obtained by upsetting the original bar material (strain 0 to 1) and an extension obtained by upsetting the pre-strained material (strain >1).

3.4 Relationship between microhardness and flow stress

The flow stress (0.2% offset) and the microhardness increase with the applied strain. At large strain the ratio between the two values is constant, see Fig. 6, in agreement with previous work (Meyers and Chawla, 2009; Zhang et al., 2012a). For lower strains, a conversion from hardness to flow stress must be determined. The ratio between hardness (MPa) and flow stress (MPa) decreases as the strain increases from 0 to 0.31, while a further increase in strain reduces the ratio gradually up to a strain of 0.96, above which the ratio becomes constant at 3.5, as shown in Fig. 6. The experimental data are fitted by the relationships:

$$HV = 7.4 - 16.31 \times \sigma + 15.56 \times \sigma^2 \qquad \varepsilon : 0 - 0.31 \tag{3a}$$

$$HV = 4.08 - 0.87 \times \sigma + 0.28 \times \sigma^2 \qquad \varepsilon : 0.31 - 0.96 \tag{3b}$$

$$HV = 3.5 \times \sigma \qquad \varepsilon > 0.96 \tag{3c}$$

where HV is the microhardness, σ is the flow stress and ε is the compressive strain corresponding to equivalent strain.

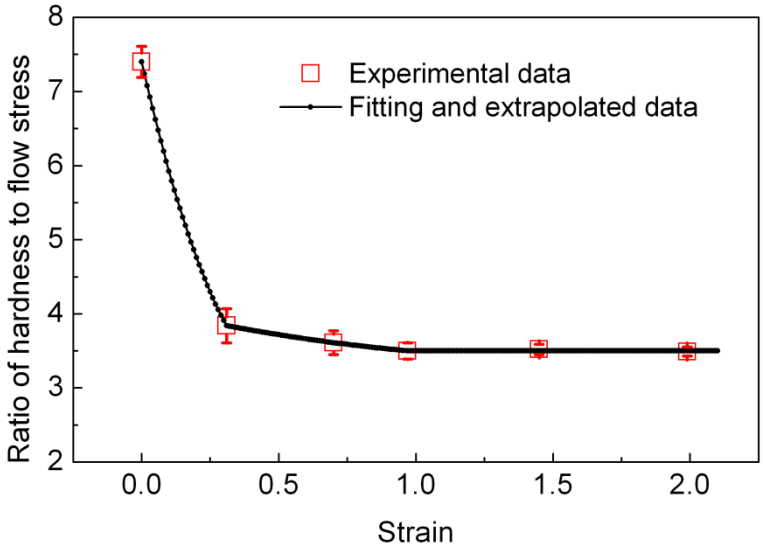

Figure 6. Ratio of hardness to flow stress (0.2% offset) versus the compressive strain.

3.5 Deformed microstructure

The microstructure evolves with increasing strain to a finer and finer scale as grains are subdivided by dislocation boundaries at small and medium strains supplemented with high angle boundaries (≥ 15°) at large strains. Boundaries form cell block which are a contiguous groups of dislocation cells in which the same set of glide systems operate (Hughes and Hansen, 1995). With increasing strain these cell blocks rotate towards the compression plane and form the typical lamellar structure with extended boundaries parallel to the compression plane and short interconnecting boundaries between the lamellar boundaries (see Fig. 7d). This structure is homogeneous but at medium and large strains it can be intersected by S-bands which are coarse slip bands that intersect parallel groups of extended boundaries. Other features are microbands and dense dislocation walls (Hughes and Hansen, 1995).

This evolution is shown in Fig. 7 by EBSD micrographs together with inverse pole figures. The structural evolution follows the universal pattern for grain subdivision (Hughes and Hansen, 2004). The deformation microstructure at strains of 0.96 and 1.90 observed by transmission electron microscopy (TEM) shows similar characteristics as those characterized by EBSD (Fig. 8), in support of using EBSD to quantify the microstructural parameters in the present work.

The original sample before compression has a strong <001> texture with a few <111> recrystallized grains (Fig. 7a). During compression, the initial texture poles in the contoured inverse pole figures with the axis parallel to the compression direction, move towards <110> pole from both <001> and <111> poles along <001>_<110> and <111>_<110> (Fig. 7a), and finally a strong <110> fiber texture has developed (Fig. 7d).

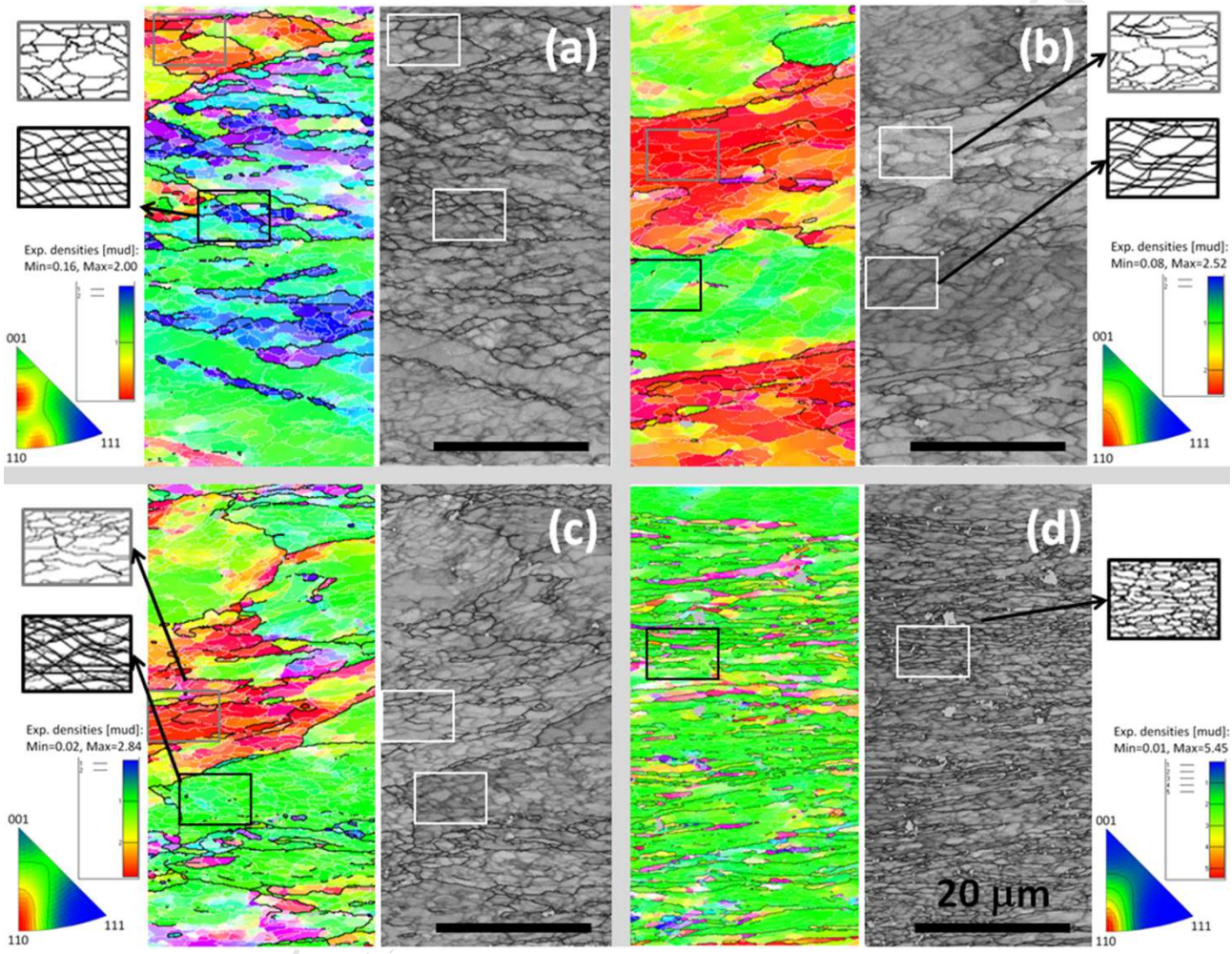

Figure 7. EBSD micrographs and sketches to show dislocation structures and inverse pole figures with the axis parallel to the compression direction of cylinders at strains of (a) 0.7, (b) 0.96, (c) 1.44 and (d) 1.9. The micrographs in the inverse pole figure (IPF) coloring and band contrast (BC) grey coloring are shown seperately to reveal the details of deformation structure. The white lines in the colored maps represent dislocation boundaries with a misorientation angle above 1.5°, while the black lines in the colored maps are dislocation boundaries with a misorientation angle above 15°. Zero solution is shown in silver. The colored inverse pole figures show the evolution of a <110> fiber texture. The microstructure in grey-framed and black-framed areas in IPF colored micrographs and white-framed areas in BC grey micrographs in (a)-(d) are sketched in the enlarged grey-framed and black-framed boxes besides the micrographs.

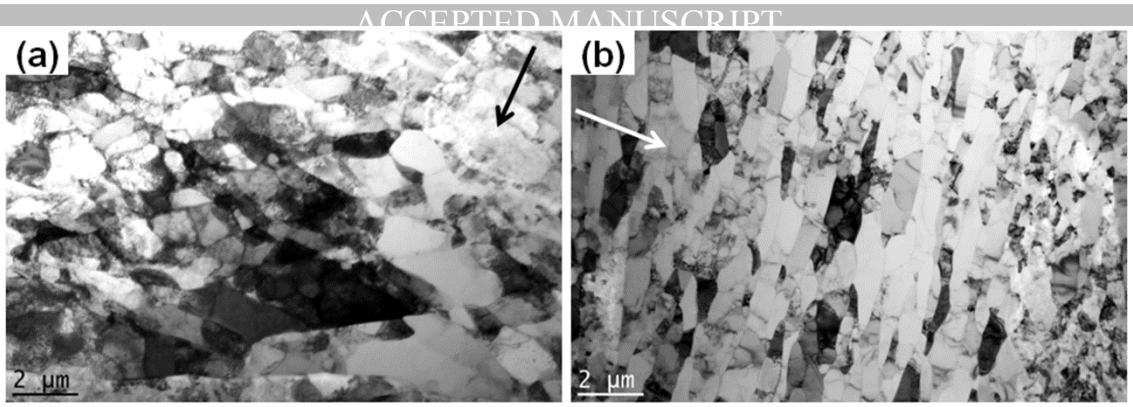

Figure 8. TEM micrographs showing the deformation structures at a strain of 0.96 (a) and a lamellar structure at a strain of 1.9 (b). The white and black arrows represent the compression direction.

3.6 Microstuctural parameters and strength

The microstructural analysis covers microstructural parameters and their evolution with strain. A universal framework of structural subdivision by dislocation boundaries and medium to high angle boundaries form the basis of this analysis assuming the deformation has been homogeneous. The two types of boundaries are: i) incidental dislocation boundaries (IDBs) formed by statistical trapping of dislocations and ii) geometrically necessary boundaries (GNBs) which delineate regions which deform either with different slip systems or with different strain partitioning on the same systems (Hughes and Hansen, 1995; Kuhlmann-Wilsdorf and Hansen, 1991; Wert et al., 2007). Certain characteristics of IDBs are synonymous with dislocation cell boundaries. In contrast GNBs are similar to grain boundaries as they separate regions of materials with different crystallographic orientations as shown by their medium to high boundary misorientation angles.

A structural characterization of the IDB/GNB structure must be based on TEM which has been used in the microstructural characterization of cold-rolled AA 1200 (Liu et al., 2002). In this study the flow stress (σ) is expressed as a superposition of Hall-Petch strengthening and Taylor strengthening as expressed:

$$\sigma - \sigma_0 = M\alpha Gb\sqrt{\left(\frac{1.5S_v\theta}{b}\right)_{IDB}} + k_{HP}\sqrt{\frac{1}{2D^{GNB}}} \quad (4)$$

k_{HP} is the slope of the straight line relating the flow stress of a polycrystalline material to the reciprocal square root of the grain size, taken to be 41 $MPa\ \mu m^{0.5}$ (Kamikawa et al., 2009). D_{GNB} is

the mean spacing between parallel GNBs measured perpendicular to the boundaries, i.e., a random spacing is $2D_{GNB}$. α is a constant taken to be 0.24, G is the shear modulus ($26\ GPa$), and b is the Burgers vector ($0.286\ nm$). θ is the misorientation angle across the IDBs and S_v is the surface area of IDBs per unit volume taken as $\frac{\pi}{2D_{IDB}}$. The surface area per unit volume of GNBs equals $1/D^{GNB}$, thus eq.(4) can be rewritten:

$$\sigma - \sigma_0 = M\alpha Gb\sqrt{(\frac{1.5S_v\theta}{b})_{IDB}} + k_{HP}\sqrt{\frac{S_v^{GNB}}{2}} \quad (5)$$

The total surface area per unit volume of GNBs and IDBs is S_v^{tot} and by introducing the surface area per unit volume of GNBs equal to f, S_v^{tot} can be expressed:

$$S_v^{tot} = S_v^{GNB}\cdot f + S_v^{IDB}\cdot(1-f) \quad (6)$$

S_v^{tot} can be taken equal to $2/D_{av}$, where D_{av} is the average spacing between boundaries measured along random lines (Underwood, 1970). This leads to the expression:

$$\frac{1}{D_{av}} = \frac{1}{D^{GNB}} + \frac{\pi}{2D^{IDB}} \quad (7)$$

Thus,

$$\sigma - \sigma_0 = \left[k_{HP}\sqrt{f} + M\alpha Gb\sqrt{\frac{3\theta^{IDB}}{b}}\right]\cdot\frac{1}{\sqrt{D_{av}}} \quad (8)$$

In the present study, the structural parameters have been determined by EBSD which does not allow a characterization of dislocation boundaries with a misorientation less than ~ 1.5°. Instead, the microstructure will be described in terms of low angle boundaries < 15° and high angle boundaries > 15° (Zhang et al., 2012) where f is the surface area per unit volume of HABs. A replacement of θ^{IDB} with θ^{LAB} in Eq. (8) and calculating the average boundary spacing by the expression:

$$\frac{2}{D_{av}} = \frac{1}{D^{HAB}} + \frac{\pi}{2D^{LAB}} \quad (9)$$

Which geives a modified Hall-Petch slope (Zhang et al., 2012a; Hansen, 2004) equal to:

$$k_2 = k_{HP}\sqrt{f^{HAB}} + M\alpha G\sqrt{3b\theta^{LAB}(1-f^{HAB})} \quad (10)$$

where k_{HP} is the Hall-Petch slope which has been determined from tensile tests of fully-recrystallized samples of pure aluminum (Kamikawa et al., 2009), $41\ MPa\ \mu m^{0.5}$. The other parameters in Eq. (6) are: the fraction of HABs (f^{HAB}), the average misorientation angle (θ^{LAB}) of LABs, the Burgers vector b (0.286 nm for aluminum), the shear modulus G (26000 MPa), the Taylor factor M taken to be 2.2 with <100> and/or <110> texture in the compression direction, α a number taken to be 0.24 and σ_0 the friction stress.

In the present aluminium AA1050, there is a small fraction of intermetallic particles (see Fig. 2) which will add to friction stress for pure aluminium (σ_{00}), thus:

$$\sigma_0 = \sigma_{00} + \sigma_{particle} \tag{11}$$

σ_0 is estimated to be ~ 32 MPa and based on Eq. (9) k_2 can be calculated to 90 ~ 109 $MPam^{0.5}$ with an average of $98 \pm 7.8\ MPa\ \mu m^{0.5}$, as shown in Table 3. The relative small standard deviation supports the assumption of a homogeneous deformation structure in the compressed cylinders. It is found that D_{av} decreases with increasing strain as shown in Fig. 9. An estimate of k_2 can also be obtained for cold rolled aluminium (Liu et al., 2002) where the IDB/GNB parameters have been determined by TEM (see Section 6.1).

Table 3. Structural parameters and tensile flow stress ($\sigma_{0.2\%}$) of compressed AA 1050

True strain	D_{av} (μm)	k_2 (MPa•μm$^{0.5}$)	σ (MPa)
0.70	1.61 ± 0.50	108.8	117.5
0.96	1.06 ± 0.30	95.9	124.6
1.44	0.85 ± 0.24	96.9	137.0
1.90	0.63 ± 0.18	90.2	145.0

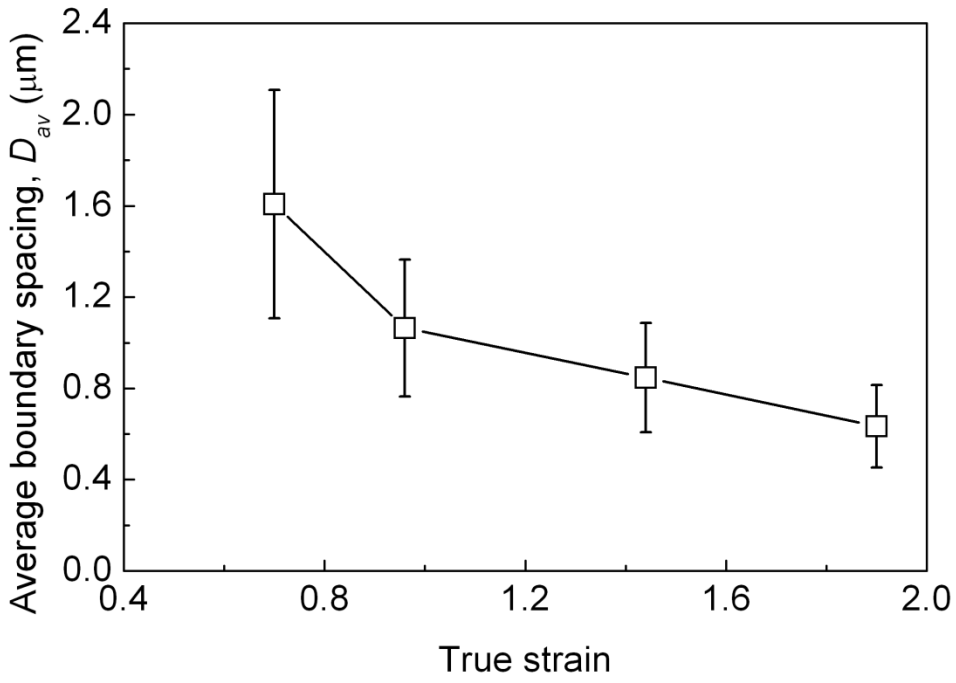

Figure 9. D_{av} versus strain for compressed cylinders

4. Heterogeneous deformation of rings

4.1 Compression tests of rings

The ring tests encompass two rings: Ring 1 machined from a hot extruded bar and Ring 2 machined from the same bar after pre-straining to a strain of 1. The ring test is carried out with the objective of inducing a high degree of heterogeneous deformation, and the friction between the tool and the workpiece is maximized by choosing rough tools and poor lubrication. The tool was ground rotationally by a 220# stone to a mean roughness $R_a = 0.48\ \mu m$. Kerosene, which is commonly used for cleaning purposes, is used as a lubricant. The initial rings are made with the typical $D_0 : d_0 : h_0 = 6 : 3 : 2$ ratio with the outer diameter $D_0 = 18\ mm$, the inner diameter $d_0 = 9\ mm$, and the height $h_0 = 6\ mm$. The initial ring wall thickness is then 4.5 mm. The final height and final inner diameter of the compressed ring are used to calculate the height reduction,

$$R = \frac{h_0 - h_1}{h_0} \tag{12}$$

and the change in inner diameter,

$$d = \frac{d_0 - d_1}{d_0} \tag{13}$$

where d_1 and h_1 are the inner diameter of the curved inner wall surface and the final height of the compressed ring, respectively.

Fig. 10 shows the simulated calibration curves relating the decrease in inner diameter d as function of the height reduction R for different friction factors f by adopting the general friction model (Wanheim and Bay, 1978). Experimental data points are plotted on top of calibration curves showing that the frictional conditions during both ring tests are close to full sticking conditions, f = 1. For each of the two cases, the experimental points are obtained by stepwise compression to determine corresponding values of R and d. Kerosene has been reapplied before each compression step. The last experimental point (R = *54.7%* and d = *60.9%*) in Fig. 10a corresponds to the ring made from original bar material (ring 1), and the last experimental point (R = *57.8%* and d = *86.6%*) in Fig. 10b corresponds to the ring made from pre-strained material (ring 2).

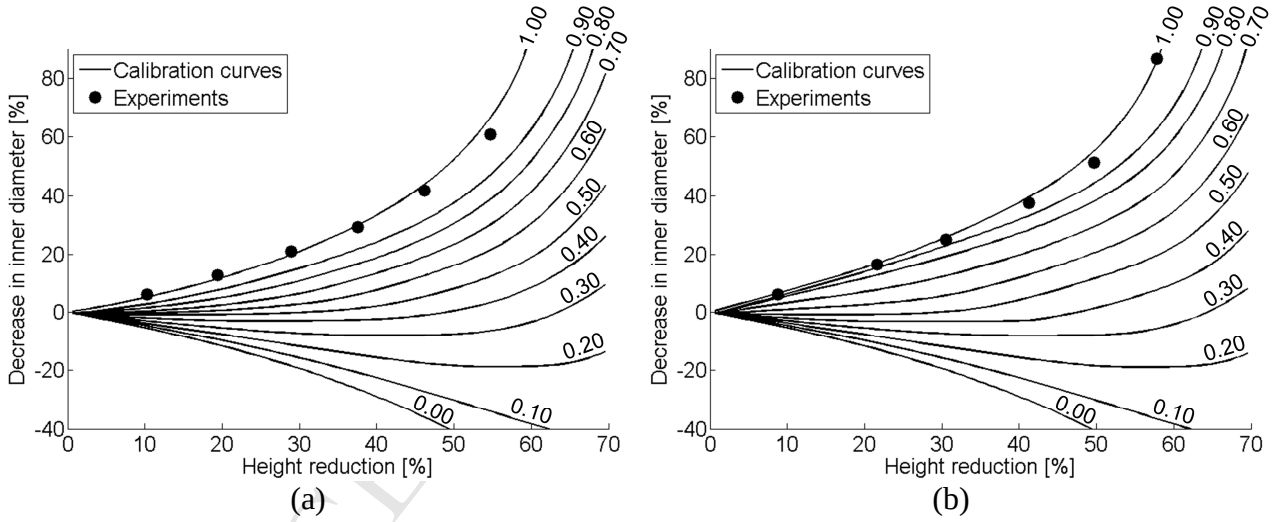

Figure 10. Simulated calibration curves with friction factor f identified on each curve and corresponding experimental data points for ring tests of Ring 1 (a) and Ring 2 (b).

4.2 Numerical simulation

The calibration curves in Fig. 10 are produced by numerical simulations with isotropic hardening which are also used in analysis of the strain and stress distributions in the ring cross-section on the assumption of isotropic hardening in a homogeneous structure. This assumption applied in an analysis of the heterogeneous deformation structures in the rings will be discussed in Section 5.2.

An axisymmetric finite element analysis has been applied with underlying calculations being built on the irreducible flow formulation, which is obtained by minimization of the following function,

$$\Pi = \int_V \bar{\sigma}\dot{\bar{\varepsilon}} dV + K \int_V \dot{\varepsilon}_v^2 dV + \int_{S_f} \left(\int_0^{|u_r|} \tau du_r \right) dS \tag{14}$$

where the energy rate due to plastic deformation is contained in the first term including the effective stress $\bar{\sigma}$ and the effective strain rate $\dot{\bar{\varepsilon}}$ integrated over the volume V. Incompressibility is enforced by the second term, where K is a penalty factor and $\dot{\varepsilon}_v$ is the volumetric strain rate. The last term includes the frictional stress τ between the tool and the workpiece by integration over the relative sliding velocity u_r on the affected surface S_f. Thereby, the material is assumed to be rigid-plastic and the tool is assumed to be perfectly rigid. For more details on the numerical implementation, see Nielsen et al., 2013. The friction model employed (Wanheim and Bay, 1978) between the workpiece material and the tool surface is:

$$\tau = f\alpha k \tag{15}$$

where f is the friction factor to be calibrated, α is the ratio of real to apparent contact area, and k is the instantaneous shear flow stress obtained by the finite element simulation with isotropic strain hardening. The real contact area α is determined by an analytical expression suitable for finite element implementation (Bay, 1987).

The cross-section of the ring see Fig. 11, is discretized by quadrilateral solid elements with two velocity degrees of freedom in each of the four nodes. The discretization is such that there are 100 elements along the height direction (Z) and 100 elements across the wall thickness of the ring in the radial direction (r). This mesh is much finer than needed for producing calibration curves, but it is needed for the later comparison with results from the microstructural analyses and the hardness measurements. The size of each element in the initial state is $60\mu m$ in height and $45\mu m$ in width.

The mechanical data obtained by simulation is not corrected for a change in crystallographic texture, which is considered not to change the analysis and conclusions significantly, taken into

account the standard deviation of local stress and strain, which are reported as effective stress and effective strain, respectively.

Fig. 11 shows an example of a finite element simulation for a ring material following the Hollomon flow stress curve $\bar{\sigma} = 126\bar{\varepsilon}^{0.23}$ (Eq. (1)), and friction between the tool and workpiece is described by a friction factor $f = 0.7$. This is an example where the friction is large enough to result in a decreasing inner diameter as the height is reduced.

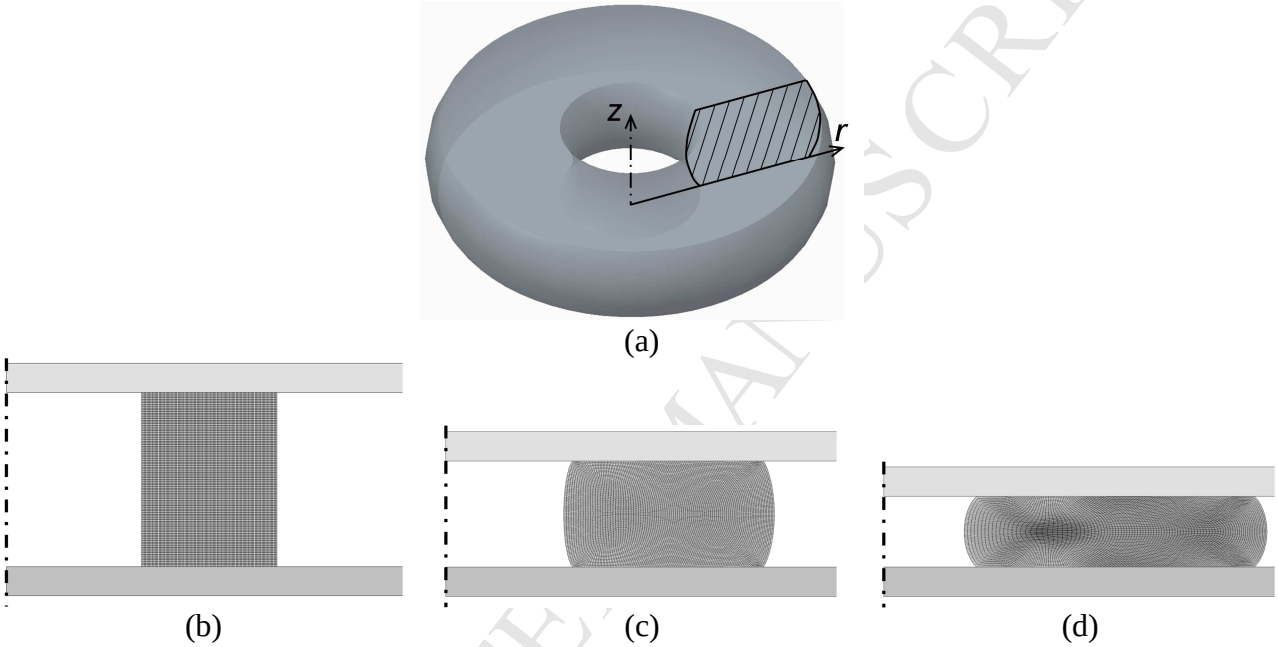

(a) (b) (c) (d)

Figure 11. Axisymmetric finite element model with isotropic strain hardening of the ring test showing (a) the simulated cross-section and definition of the coordinate system, (b) the initial mesh, (c) the deformed mesh at 40% height reduction, and (d) the deformed mesh at 60% height reduction.

Fig. 12 and Fig. 13 show the deformed mesh, the effective strain and the effective stress from numerical modelling of ring 1 and ring 2 until the compression corresponds to the final reduction achieved in the experiments. Note that the inner diameter decreases more in ring 2 than in ring 1 from the geometry despite the contact being similar full sticking in both cases. These simulations introduce the shape and size change of rings, which have been validated by reproducible compression testing of rings.

The simulations for both rings show that the friction between the tool and the ring introduces a heterogeneous stress and strain distribution reported as effective stress and effective strain. To

demonstrate this heterogeneity, seven boxed areas with edge length ~ 50 μm have been numbered 1-7 in the strain distribution figures in Fig. 12 and Fig. 13. These areas are characterized qualitatively as follows: 1 is close to the area where the material has flown inward with a folding of the inner ring wall contacting the tool surface; 2 represents inward flow, without folding against the tool surfaces; 3 represents the area close to the full sticking contact area with the tool surface; 4 represents the area where the material has mainly experienced axial compression with a radial elongation; 5 represents the outer zone with folding of material against the tool surface; 6 is characterized by axial compression with outwards radial flow; 7 represents the outward material flow of the outer ring wall without folding. Note that both rings have the high level of stress and strain in area 5.

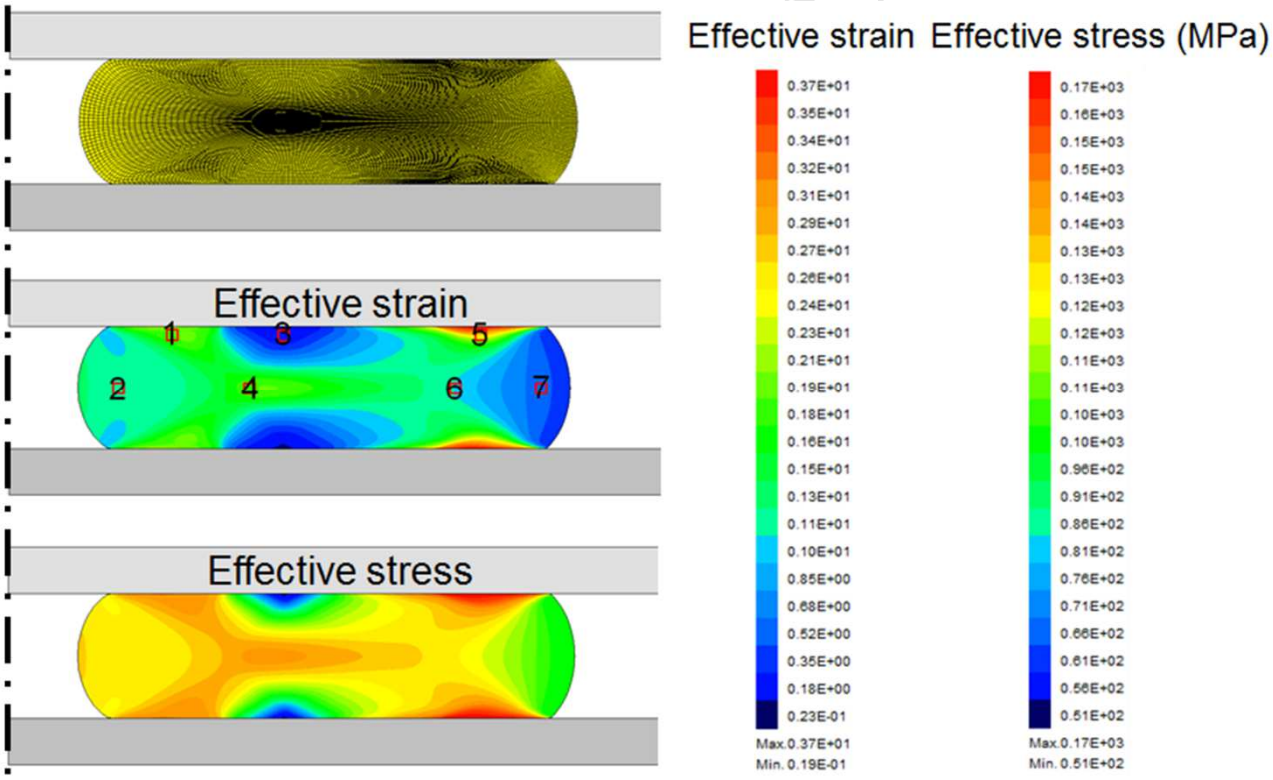

Figure 12. Deformed mesh, strain and stress distribution from FEM modelling of ring 1. Small red boxes with numbers from 1 to 7 in the effective strain distribution figure represent seven areas for the microstructural and hardness analyses in Section 4.

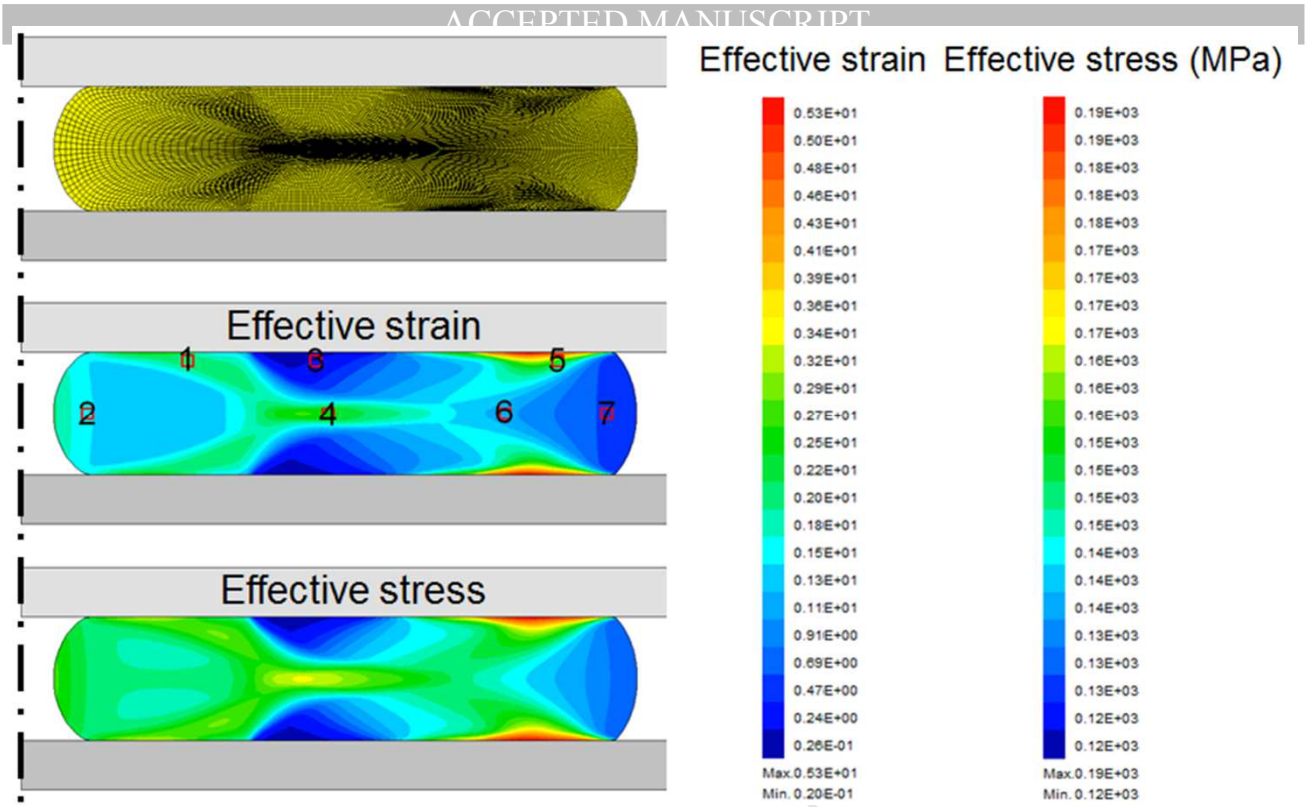

Figure 13. Deformed mesh, strain and stress distribution from FEM modelling of ring 2. Red outlined boxes with numbers from 1 to 7 in the effective strain distribution figure represent seven areas for the microstructural and hardness analyses in Section 4.

4.3 Deformation microstructure

The seven representative areas in the cross sections of ring 1 and ring 2 have been characterized by EBSD, as shown in Fig. 14 and Fig. 15. In ring 1, the heterogeneous microstructure is pronounced: (i) slightly deformed areas with the original grain shape kept and a small amount of dislocation boundaries in the grains where the sticky zone is located (Area 3, Fig. 14c); (ii) compressed original grains with elongated dislocation boundaries in the grains (Area 7, Fig. 14g); (iii) equiaxed dislocation cells in the original grains (Area 2, Fig. 14b); (iv) equiaxed subgrains surrounded by low angle dislocation boundaries (Area 1, Fig. 14a); (v) inclined dislocation cell structures with one set of dense dislocation walls (DDWs) mixed with equiaxed dislocation cells (Area 5, Fig. 14e); (vi) inclined dislocation cell structures with two sets of DDWs (Area 6, Fig. 14f); and (vii) parallel lamellar dislocation structures with localized shear in the form of S-bands which represent the typical microstructures at high strains (Area 4, Fig. 14d).

In ring 2, the microstructure is more homogeneous: (i) inclined dislocation cell structures with one set of low angle or high angle DDWs mixed with equiaxed dislocation cells (Areas 1, 5 and 7, Fig. 15a, 15e and 15g); (ii) inclined dislocation structures with one set of low angle DDWs (Area 3, Fig. 15c); (iii) equiaxed cells with low angle or high angle boundaries (Area 2, Fig. 15b); and (iv) lamellar dislocation structures with localized shear in the form of S-bands (Areas 4 and 6, Fig. 15d and 15f). These microstructural features are summarized in Table 4.

Table 4. Microstructural morphology in compressed rings

Microstructural morphology		Ring 1	Ring 2
I	A small amount of dislocation boundaries in the original grains	Area 3, Fig. 14c	-
II	Elongated dislocation boundaries in compressed original grains	Area 7, Fig. 14g	-
III	Equiaxed dislocation cells	Area 2, Fig. 14b	Area 2, Fig. 15b
IV	Equiaxed subgrains surrounded by low angle dislocation boundaries	Area 1, Fig. 14a	-
V	Inclined dislocation cell structures with one set of DDWs mixed with equiaxed dislocation cells	Area 5, Fig. 14e	Area 1, 5 and 7, Fig. 15a, 15e and 15g
VI	Inclined dislocation cell structures with two sets of DDWs	Area 6, Fig. 14f	-
VII	Parallel lamellar boundary structures showing localized shear (S-bands)	Area 4, Fig. 14d	Area 4 and 6, Fig. 15d and 15f
VIII	Inclined dislocation structures with one set of low angle DDWs	-	Area 3, Fig. 15c

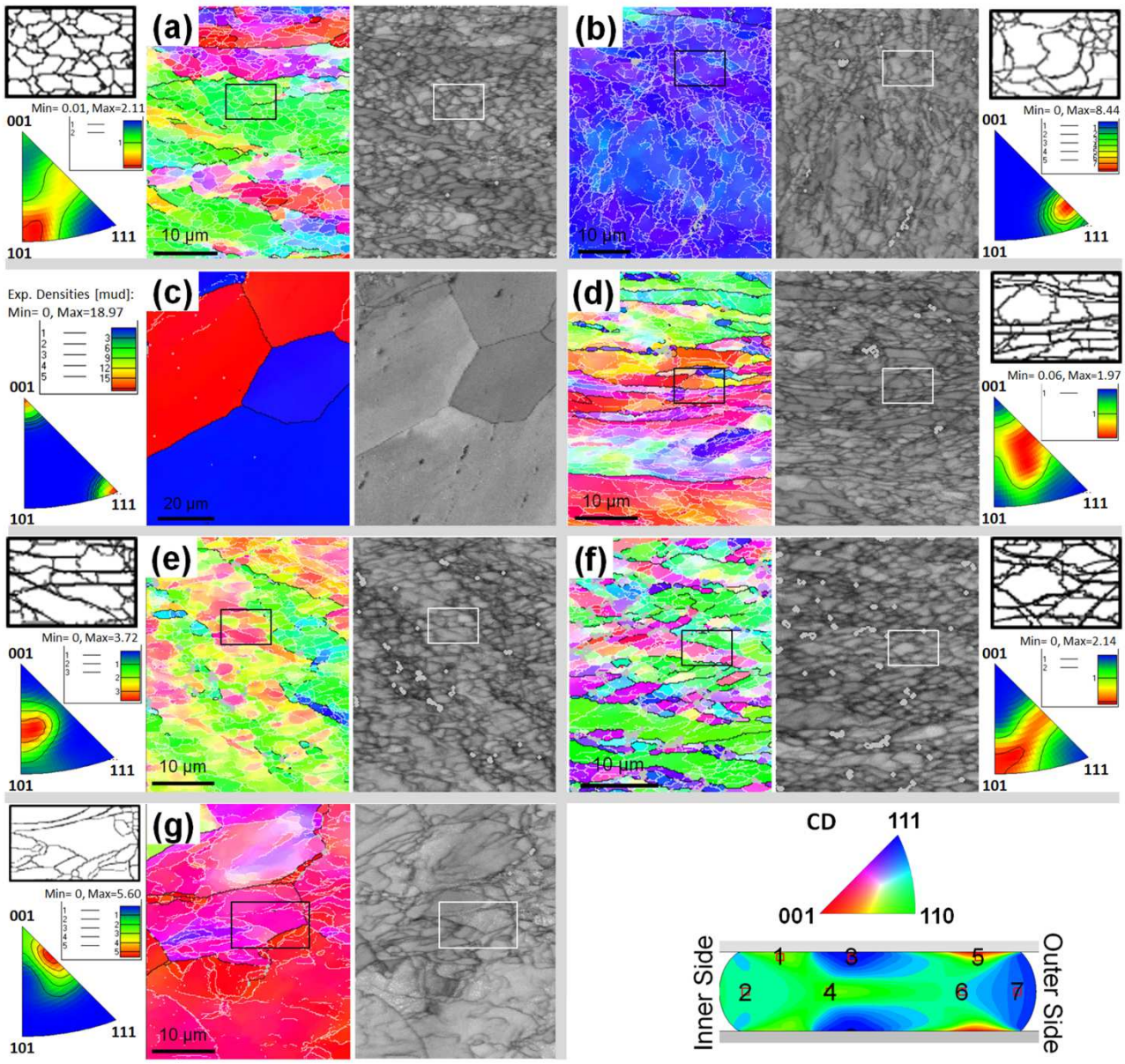

Figure 14. EBSD micrographs and sketches showing dislocation structures and inverse pole figures of the microstructure in ring 1. (a)-(g) show, respectively, the microstructure of Areas 1-7 sketched in the strain distribution map of the ring cross section (Fig. 12). The micrographs are in the inverse pole figure (IPF) coloring with the axis parallel to the compression direction and band contrast (BC) grey coloring separately to reveal the details of boundaries. The white lines in IPF colored maps represent dislocation boundaries with misorientation angle above 1.5°, while the black lines in IPF colored maps are dislocation boundaries with misorientation angle above 15°. Zero solution is shown in silver. The contoured inverse pole figures with the axis parallel to the compression direction. The dislocation boundary structures in black-framed areas in IPF colored maps and white-framed areas in BC colored maps are sketched in the enlarged black-framed boxes besides the EBSD micrographs. CD represents the compression direction.

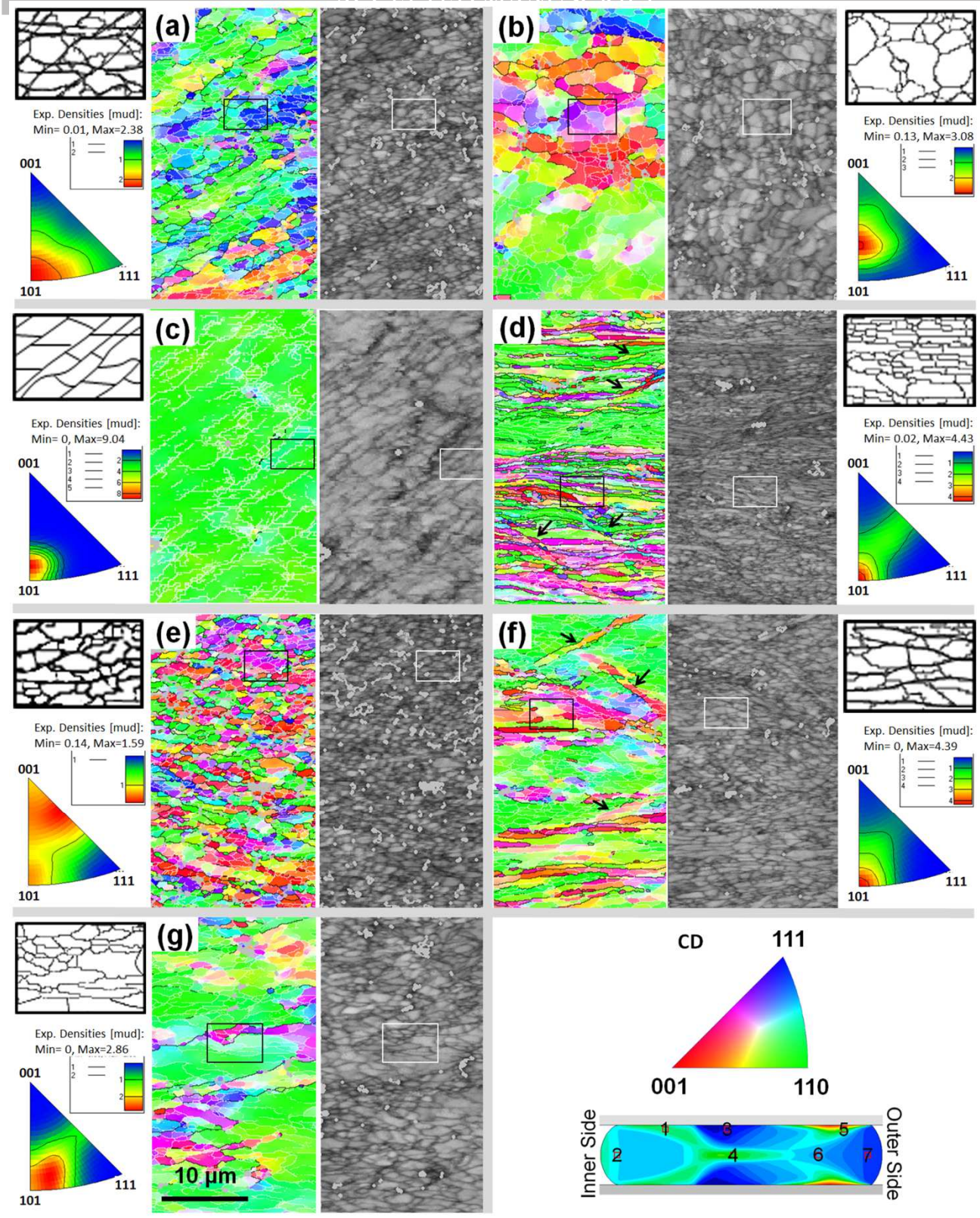

Figure 15. EBSD micrographs and sketches showing dislocation structures and inverse pole figures of the microstructure in ring 2. (a)-(g) show, respectively, the microstructure of Areas 1-7 sketched in the strain distribution map of the ring cross section (Fig. 13). The black arrows show the localized in the form of s-bands in the microstructure in (d) and (f). For an extended figure caption, see Figure 14.

4.4 Microhardness

The microhardness matrix is used on the electro-polished cross section. As seen in Fig 16, this matrix does not reach the top and bottom surface for two reasons: (i) the microhardness indent has a size with a diagonal about 20 μm and some distance must be kept to the surface and (ii) the edges of top/bottom surfaces cannot be kept at 90° as there are always wrinkles close to the edges where both surfaces have been covered with chemicals protecting them during electropolishing. The distribution of hardness values in Fig. 18 is obtained within an area which allows a direct comparison with FEM values in Fig. 12 and Fig. 13. For ring 1 the hardness is in the range 32.4 ~ 53.6 kg/mm^2, and for ring 2 the range is from 37.9 kg/mm^2 to 55.1 kg/mm^2. These results support the selection of seven representative areas shown in Fig. 12 and 13 based on FEM to be discussed in the following. However, it should be noted that 100% agreement of symmetry and distribution between the hardness and simulation is very difficult to obtain for two reasons: 1) local inhomogeneous flow by local shear and observed as S-bands cannot be captured by the present simulation; 2) inclusions can introduce a microhardness difference around 3 which can significantly change the color marking in Figure 16.

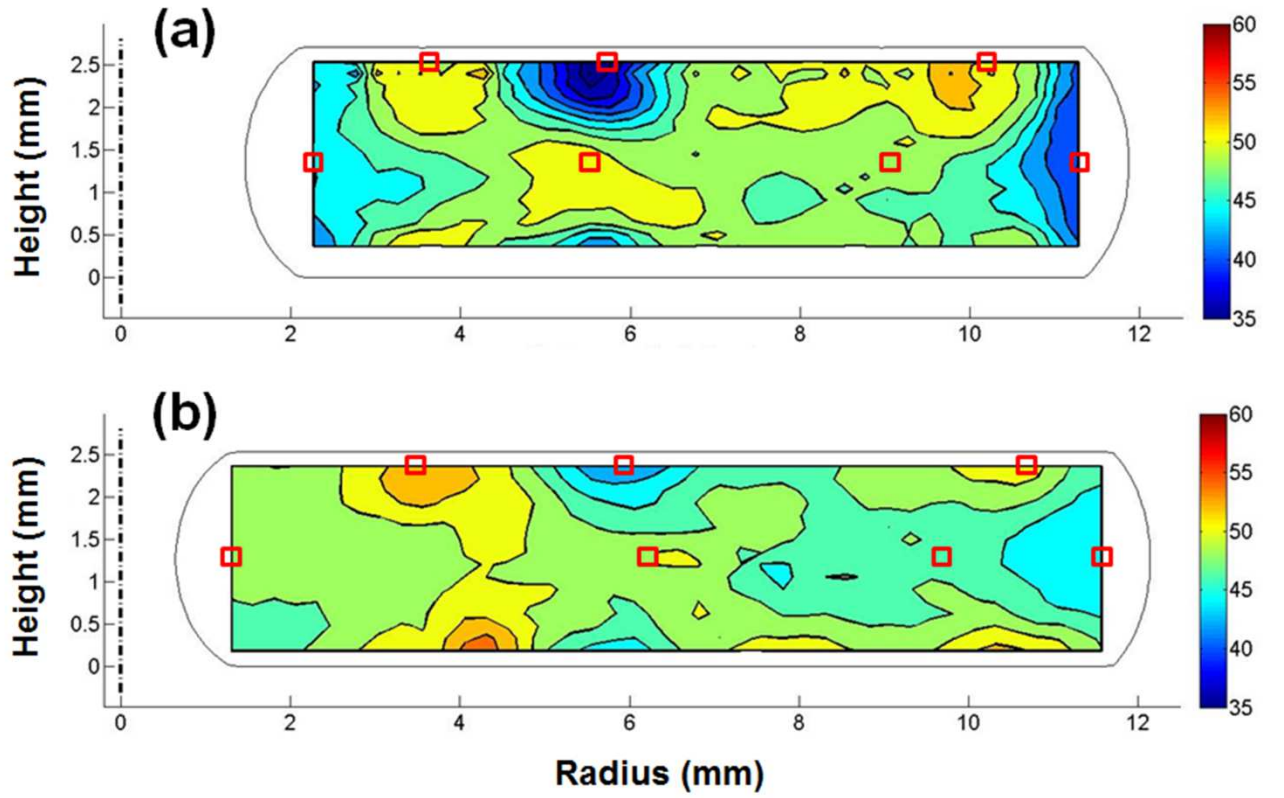

Figure 16. Microhardness (HV 0.05) distribution in the rings: (a) ring 1 and (b) ring 2. The hardness matrix for ring 1 is 17×37 with spacings between neighboring indents: 0.135 mm for rows and 0.25 mm for columns; while that for ring 2 is 16×42 with spacings between neighboring indents: 0.145 mm for rows and 0.25 mm for columns. The black outlines are the cross sections of rings analyzed by FEM and compressed experimentally. The seven red squares represent the seven areas shown in Figs. 12 and 13.

5. Strength analysis

An estimate of the mechanical behavior of seven areas in each of the two rings has been obtained by applying microhardness measurement, quantitative microstructural analysis and finite element simulation. For a comparison and validation of the three techniques we derive the flow stress of each of the 14 areas in the two rings and corresponding plastic strains.

5.1. Flow stress and microhardness

The flow stress is calculated from the microhardness measurements based on Eq. (3) and will be reported as $\sigma_{hardness}$ together with the plastic strain obtained by simulation, ε_{sim}, in Tables 5 and 6.

Table 5. Microhardness (Fig. 16), calculated flow stresses from hardness ($\sigma_{hardness}$), and simulated strains in ring 1 as shown in Fig. 12.

Area	2	1	4	3	6	5	7
Strain (Simul.)	1.06	1.8	1.84	0.03	1.13	2.55	0.41
HV (kg/mm^2)	46.5 ± 3	52.1 ± 3	51.2 ± 3	32.7 ± 3	47.3 ± 3	49.9 ± 3	37.9 ± 3
$\sigma_{hardness}$ (MPa)	130.2 ± 8.4	145.9 ± 8.4	143.4 ± 8.4	46.3 ± 4.2	132.4 ± 8.4	139.7 ± 8.4	98.4 ± 7.8

Table 6. Microhardness (Fig. 16), calculated flow stresses from hardness ($\sigma_{hardness}$), and simulated strains in ring 2 as shown in Fig. 13.

Area	2	1	3	4	6	5	7
Strain (Simul.)	2.44	2.99	1.02	3.37	2.01	2.91	1.41
HV (kg/mm^2)	48.7 ± 3	52.6 ± 3	41.7 ± 3	49.9 ± 3	48.1 ± 3	51.2 ± 3	47.3 ± 3
$\sigma_{hardness}$ (MPa)	124.8 ± 10	144 ± 12	108.2 ± 8.3	144 ± 11.9	130.5 ± 10.6	136.6 ± 11.2	136.1 ± 11.1

5.2. Flow stress and microstructure

In Section 3.6 for homogeneously deformed aluminium the flow stress was expressed as: $\sigma - \sigma_0 = k_2 {D_{av}}^{-0.5}$, where D_{av} is the average spacing between LABs and HABs. The microstructure in the fourteen areas however differs in morphology when compared with compression structures (see Fig. 8). However individual structural features are comparable (see Table 4, and Figs 14 and 15), illustrating structural subdivision by different types of boundaries with misorientation angles ≤ 15° and > 15°. For these structures, the boundary spacing has been determined by EBSD and classified as (i) low and medium angle dislocation boundaries (LABs) with a misorientation angle < 15° and (ii) high angle boundaries (HABs) with a misorientation angle > 15°. Based on the average spacing between these boundaries D_{av}, the flow stress is calculated in accordance with Eq. (11) and reported in the tables as σ_{cal}. The three flow stress values given in Table 7 and Table 8 have been obtained based on different methods and assumptions, and are therefore not directly comparable. However, considering that the standard deviation of the flow stress values is about 10% or less, they may be validated by a simple comparison.

Table 7. Simulated strain, flow stress from hardness ($\sigma_{hardness}$), calculated flow stress (σ_{cal}) and simulated flow stress (σ_{simul}) of seven representative areas in ring 1 (see Fig. 14).

Area	2	1	4	3	6	5	7
ε_{simul}	1.06	1.8	1.84	0.03	1.13	2.55	0.41
$\sigma_{hardness}$ (MPa)	130.2 ± 8.4	145.9 ± 8.4	143.4 ± 8.4	46.3 ± 4.2	132.4 ± 8.4	139.7 ± 8.4	98.4 ± 7.8
σ_{cal} (MPa)	127.3 ± 7.6	132.2± 8.0	145.5 ± 9.1	-	137.9 ± 8.5	138.7 ± 8.5	120.8 ± 7.1
σ_{simul} (MPa)	127.7	144.2	145	54.9	129.6	156.3	102.6

Table 8. Simulated strain, flow stress from hardness ($\sigma_{hardness}$), calculated flow stress (σ_{cal}) and simulated flow stress (σ_{simul}) of seven representative areas in ring 2 (see Fig. 16).

Area	2	1	3	4	6	5	7
ε_{simul}	2.44	2.99	1.02	3.37	2.01	2.91	1.41
$\sigma_{hardness}$ (MPa)	124.8 ± 10	144.0 ± 12.0	108.2 ± 8.3	144 ± 11.9	130.5 ± 10.6	136.6 ± 11.2	136.1 ± 11.1
σ_{cal} (MPa)	141.5 ± 8.7	151.8 ± 9.6	125.4 ± 7.5	160.4 ± 10.2	156.8 ± 10.0	150.7 ± 9.5	143.0 ± 8.9
σ_{simul} (MPa)	154.7	162.1	126.6	166.6	148	161.1	136.4

The analysis of the data in Table 7 and Table 8 shows both for ring 1 and ring 2 that the three techniques give results which follow the same trend. However the data also show differences to be discussed in the following.

Considering the numerical compression strain in ring 1 and ring 2, large differences are found when applying numerical simulation (ε_{simul}). For ring 1, the maximum strain is 2.55 (area 5); for ring 2, the maximum strain is 3-3.4 (area 1, 4 and 5), much higher than the nominal strain. A comparison with Fig. 12 and 13 shows the high stress and strain concentration in area 5 which appears as a "hot spot". For area 5 (ring 1) and area 1, 4, and 5 (ring 2), σ_{simul} is high in the range from 156.3 MPa to 166.6 MPa, which is significantly larger than $\sigma_{hardness}$ and σ_{cal}, where the range is 136.6 - 144 MPa for $\sigma_{hardness}$ and 138.7 - 160.4 MPa for σ_{cal}. This apparent overprediction of σ_{simul} may partly have its cause in the application of Eq. (3) and Eq. (4) covering both stage III and stage IV. These equations may not fully take into account that the strain hardening in stage IV may decrease with increasing strain to almost nil at very large strains. By using Eq. (3) and (4) a certain over prediction of the flow stress (σ_{simul}) in ring 2 must be expected as observed.

The structural evolution in Fig. 14 and Fig. 15, shows typical structural features which also characterize the deformation structures in compressed cylinders. However, in the highly strained areas 4 and 6, localized glide is observed in the form of S-bands, see Table 4, showing the existence

of S-bands in area 4 for ring 1 and areas 4 and 6 in ring 2. It is noteworthy that for these three areas there is good agreement between σ_{simul} and σ_{cal}. This finding indicates that localized glide in the deformation microstructure increases the strength through a structural refinement.

A comparison of techniques also shows significant differences when comparing area 5 and 7 with the other areas. In these two areas σ_{simul} is respectively larger and smaller than σ_{cal}. Between the two areas there are also large differences. Taking Ring 1 as example, the difference for σ_{simul} is 53.7 MPa compared to σ_{cal} 17.9 MPa. These observations point to strain accommodation as an important mechanism expected to be pronounced when the plastic deformation is heterogeneous. Accommodation mechanisms are dynamic or static recovery which may readily take place in aluminum characterized by a high stacking fault energy and a low melting point.

In conclusion, Table 7 and Table 8 show for almost all the chosen positions that there is good agreement between σ_{cal} and σsimul if the difference is below 10%, taken into account the standard deviation. As microscopy and simulation are complementary techniques and together cover multiple length scales, this agreement supports the use of both techniques when analyzing heterogeneous structures.

6. Discussion

Evolution of microstructure and mechanical properties during plastic deformation has been investigated extensively in aluminum over several length scales from the sample scale (~ 10 mm) to the microscopic dimensions (~ several hundred nanometers). In the present study, this is reflected in the choice of experimental techniques from hardness testing, numerical simulation to electron microscopy. To allow an in-depth analysis only one material has been selected (AA1050) in the hot-rolled condition. This material has been deformed heterogeneously in ring tests under full sticking conditions. We have chosen to compare the results of such ring tests with observations obtained for aluminum homogeneously deformed by compression and cold rolling (Liu et al., 2002). This is because the deformation microstructure and mechanical behavior of fcc metals like aluminum has been analyzed based on universal hypotheses and fundamental principles (Hughes and Hansen 2004) which we shall apply in the analysis of the compressed rings. The discussion is therefore

divided in sections: 6.1 homogeneous deformation of Al; 6.2 ring tests and their validation; 6.3 methodology and outlook.

6.1. Homogeneous deformation of Al

The microstuctural evolution during plastic deformation of aluminum can be characterized as a structural subdivision on a finer and finer scale as the strain is increased. Subdividing boundaries are low, medium and high angle boundaries forming different structural morphologies, for example, cells and subgrains delineated with low and medium angle dislocation boundaries and lamellar structures where medium and high angle boundaries subdivide the structure. Based on the characteristics of the boundaries, the LEDS (low energy dislocation structure) principle has been applied on an analysis of their formation and evolution (Kuhlmann-Wilsdorf 1989a; Kuhlmann-Wilsdorf 1989b). According to this principle dislocations in a boundary or cell structures are favored over a random distribution of dislocations due to a reduction in the line energy per unit length of dislocation lines. In parallel, long range stress fields are reduced which have recently been observed in aluminum by three dimensional X-ray diffraction utilizing synchrotron radiation (Levine et al., 2006). The flow stress is expressed as a sum of dislocation strengthening and Hall-Petch strengthening taking the average boundary spacing D_{av} as the sole strengthening parameter, not taken into account that dislocation strengthening is isotropic and Hall-Petch strengthening can be anisotropic. D_{av} has in Section 3.6 been obtained as an empirical parameter based on an analysis of the homogeneously deformed cylinder. However, besides being empirical, this parameter can be derived based on physical mechanisms as dislocation and boundary strengthening (see Section 3.6). D_{av} is therefore considered an acceptable parameter for an analysis by EBSD of the local flow stresses in the 14 areas in the compressed rings. This follows our hypothesis suggesting that small local regions in a heterogeneous microstructure can be analyzed in parallel with the analysis of a macroscopic homogeneous deformation structure. This experimental basis is therefore expanded by including structural data obtained by TEM of aluminum AA 1200 (99%) (Liu et al., 2002) which has been homogeneously deformed by cold rolling to high strain.

The relationship between the flow stress (0.2% offset) versus the reciprocal square root of D_{av} is shown in Fig. 17 for compressed and cold rolled aluminum. A linear relationship for small values of D_{av} is extrapolated to a value for $\sigma_0 + \sigma_{particle}$ (see Eq. (13)), taken to ~ 30 MPa. In this plot, k_2 equals to 98 $MPa \cdot \mu m^{0.5}$, in good agreement with the analysis in Section 3.6 (Table 3).

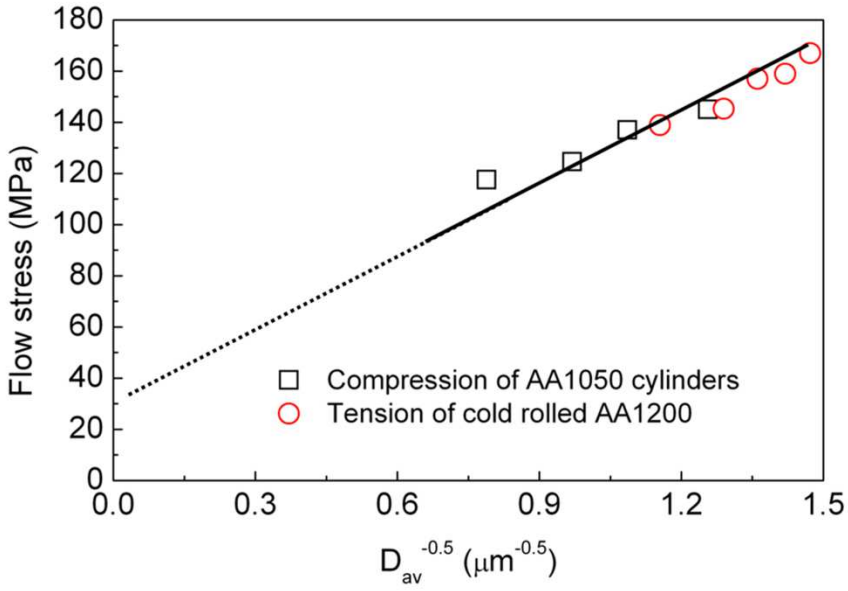

Figure 17. Flow stress versus the reciprocal square root of D_{av}

To obtain corresponding data for local stress and strain, the relationship between $1/D_{av}$ is plotted in Fig. 18 versus the strain showing a bilinear relationship reflecting the change in hardening rate at an intermediate strain, parabolic hardening (stage III) to linear hardening (stage IV), in accordance with Fig. 5.

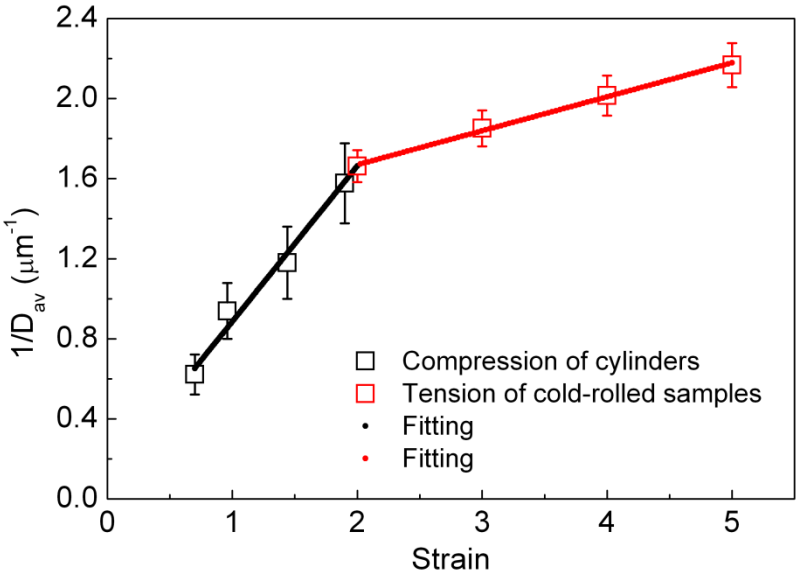

Figure 18. $1/D_{av}$ versus strain

6.2. Ring tests and their validation

The compressed rings demonstrate a very heterogeneous microstructure which raises the problem of how to choose representative areas for analysis. Based on an inspection of the surface of the deformed rings and the change in sample geometry during compression, significant heterogeneities have evolved in the structure. We have identified seven areas in each ring for further analysis. This choice is based on the numerical simulation which also shows significant variations between the chosen areas.

For 13 areas (excluding area 3 for ring 1) the microstructural analysis allows corresponding values of stress and strain to be estimated based on Fig. 17 and Fig. 18. The 13 data points show a significant spread but a fitted curve shows the typical work hardening behavior for a fcc metal, see Fig. 5. Fig. 19 shows a high work hardening rate at small to medium strain (stage III) followed by a stage of low work hardening rate (stage IV). A comparison of Fig. 19 and Fig. 5 shows that for the hardening rate there is good agreement in absolute values. Also by approximating stage IV, a linear relationship for the slope is $6.1 \times 10^{-4}\ G$ in Fig. 19 and $5.8 \times 10^{-4}\ G$ in Fig. 5. The good agreement that local stress and strain in small regions of a heterogeneous structure can be analyzed as the region has been homogeneously deformed. This hypothesis may also rationalize the assumption of isotropic hardening in the numerical simulation and is underpinned by the finding of a good agreement between σ_{calc} and σ_{sim} (see Table 7 and 8).

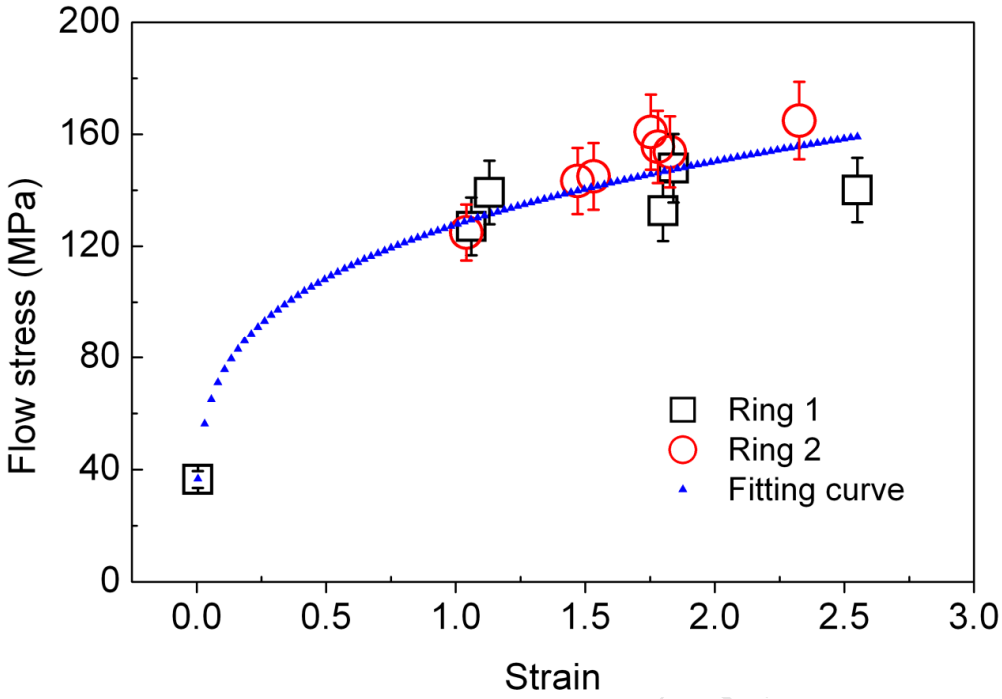

Figure 19. σ_{calc} versus ϵ_{calc}. The fitting curve follows $\sigma = 127.7\epsilon^{0.23}$.

6.3. Methodology and outlook

The comparison of results using three different techniques points to a combination of a structural analysis with a FEM analysis on different length scales depending on the problem to be investigated. In the present study the problem has been interacting between a tool and a metal where the microstructural analysis can be extended to a very small scale capturing different types of heterogeneities as localized glide in macro- and micro- shear bands and high concentration of shear and/or strain in hot spots or near cracks. An extension in length to such ultrafine microstructure will require additional characterization techniques such as nanoindentation and transmission electron microscopy. Also to be included is three dimensional X-ray diffraction using synchrotron radiation with fine spatial resolution. Complementary to these characterization techniques, CPFEM can be extended to a small structural scale including texture and boundary effects and MD modelling which extend the scale further. Therefore combination of experimental characterization and modelling is promising and examples are the combination of crystal plasticity models for polycrystalline aggregate (Bronkhorst, et al., 1992; Bulter and McDowell, 1998; Sarma and Dawson, 1996) and finite element methods (Bhattacharyya et al., 2001; Jung et al., 2013) to further

understanding of through-thickness macro-texture evolution and local texture gradients (Huh et al., 2004) and the accompanying anisotropic properties of rings during compression under high friction conditions. A detailed analysis of strain gradients, strain rate gradients, material flow velocity gradients and localization phenomena (Bontcheva and Todorov, 1992) may also be included.

7. Conclusions

The heterogeneities in strength, strain and microstructure caused by friction during metal forming is investigated by compression of Al rings. These tests are underpinned by an analysis of Al cylinders homogeneously deformed by compression. The conclusions are the following.

1. For compressed cylinders the macroscopic stress and strain relate to the boundary spacing D_{av} and the boundary area per unit volume $S_v = 2/D_{av}$ where D_{av} is the average spacing between deformation induced low angle boundaries and high angle boundaries (>15°) indistinguishable from grain boundaries. The flow stress can be expressed by a Hall-Petch formulation where the strength contribution from all boundaries is $k_2 {D_{av}}^{-0.5}$ where k_2 is a constant and $1/D_{av}$ depends on the equivalent strain as expressed in a bilinear relationship (see Fig. 18).
2. The compressed rings showed large variations in stress, strain and microstructure when characterized by three complementary techniques: microhardness testing, electron microscopy (EBSD) and FEM. Results for 14 areas (50×50 μm^2) in two rings follow the same trend with good agreement between the local stress and strain when calculated based on D_{av} quantified by EBSD or simulated by a FEM analysis.
3. The comparison of the microstructural analysis and the simulation shows the strength of using complementary characterization techniques when analyzing a heterogeneous structure with structural variations covering multiple length scales. The comparison also supports the hypothesis that the microstructure in local regions of a heterogeneous structure evolves in

accordance with universal principles established for homogeneously deformed polycrystalline metals.

Acknowledgements

The authors would like to thank The Danish Council for Independent Research (Grant number: DFF-1335-00230) for financial support. Paulo Martins would also like to thank Fundação para a Ciência e a Tecnologia of Portugal and IDMEC under LAETA - UID/EMS/50022/2013.

References

Bay, N., 1987. Friction stress and normal stress in bulk metal-forming processes. Journal of Mechanical Working Technology 14, 203-223.

Belov, N.A., Aksenov, A.A., Eskin, D.G., 2002. Iron in Aluminium Alloys: Impurity and Alloying Element. CRC Press.

Bhattacharyya, A., El-Danaf, E., Kalidindi, A.R., Doherty, R.D., 2001. Evolution of grain-scale microstructure during large strain simple compression of polycrystalline aluminum with quasi-columnar grains: OIM measurements and numerical simulations. Int. J. Plasticity 17, 861-883.

Bontcheva, N., Todorov, S., 1992. Numerical investigation of plastic localization bands in aluminium rings subjected to static axial compression. Int. J. Plasticity 8, 893-901.

Bronkhorst, C.A., Kalidindi, S.R., Anand, L., 1992. Polycrystalline plasticity and the evolution of crystallographic texture in FCC metals. Phil. Trans. R. Soc. Lond. A341, 443.

Bulter, G.C., McDowell, D.L., 1998. Polycrystal constraint and grain subdivision. Int. J. Plasticity 14, 703.

Chen, S.-L., HU, J., Zhang, X., Dong, H., Cao W., 2015. High Ductility and Toughness of a Micro-duplex Medium-Mn Steel in a Large Temperature Range from -196 °C to 200 °C. Journal of Iron and Steel Research International 22, 1126–1130.

Fan, G.H., Wang, Q.W., Du, Y., Geng, L., Hu, W., Zhang, X., Huang, Y.D., 2014. Producing

laminated NiAl with bimodal distribution of grain size by solid–liquid reaction treatment. Materials Science and Engineering A 590, 318-322.

Hansen, N., 2004. Hall–Petch relation and boundary strengthening. Scripta Mater 2004, 51:801–806.

Hughes, D.A., Hansen, N., 1995. High angle boundaries and orientation distributions at large strains. Scripta Metall. Mater. 33, 325–321.

Hughes, D.A., Hansen, N., 2004. Plastic deformation structures, ASM Handbook, ASM International, Materials Park, Ohio, USA, p. 192.

Huh M.Y., Lee K.R., Engler O., 2004. Evolution of texture and strain states in AA3004 sheet during rolling with a dead block. Int. J. Plasticity 20, 1183-1197.

Jung, K-H., Kim, D-K., Im, Y-T., Lee, Y-S., 2013. Prediction of the effects of hardening and texture heterogeneities by finite element analysis based on the Tylor model. Int. J. Plasticity 42, 120-140.

Kamikawa, N., Huang, X., Tsuji, N., Hansen, N., 2009. Strengthening mechanisms in nanostructured high-purity aluminium deformed to high strain and annealed. Acta Mater 57, 4198–4208.

Kuhlmann-Wilsdorf, D., 1989a. Theory of plastic deformation - properties of low energy dislocation structures. Mater. Sci. Eng. A 113, 1–41.

Kuhlmann-Wilsdorf, D., 1989b. Strengthening through LEDS. Strength of Metals and Alloys (ICSMA 8) 1, 221–226.

Kuhlmann-Wilsdorf, D., Hansen, N., 1991. Geometrically necessary, incidental and subgrain boundaries. Scripta Metall Mater. 25, 1557-1562.

Levine L.E., Larsen B.C., Yang W., Kassner M.E., Tischler J.Z., Delos-reyes M.A., Fields R.J., Liu W., 2006. X-ray microbeammeasurements of individual dislocation cell elastic strains in deformed single-crystal copper. Nature Mater. 5, 619-622.

Liu, Q., Huang, X., Lloyd, D.J., Hansen, N., 2002. Microstructure and strength of commercial

purity aluminium (AA 1200) cold-rolled to large strains. Acta Mater. 50, 3789-3802.

Meyers, M.A., Chawla, K.K., 2009. Mechanical behavior of materials. Cambridge, UK: Cambridge University Press p. 223–224.

Nielsen, C.V., Zhang, W., Alves, L.M., Bay, N., Martins, P.A.F., 2013. Modeling of thermoelectro-mechanical manufacturing processes with applications in metal forming and resistance welding. Springer-Verlag, London, UK.

Nikas, D., Zhang, X., Ahlström, J., 2018. Evaluation of local strength via microstructural quantification in a pearlitic rail steel deformed by simultaneous compression and torsion. Materials Science & Engineering A 737, 341-347.

Pandey, A., Khan, A.S., Kim, E.-Y., Choi, S.-H., Gnäupel-Herold, T., 2013. Experimental and numerical investigations of yield surface, texture, and deformation mechanisms in AA5754 over low to high temperatures and strain rates. Int. J. Plasticity 41, 165-188.

Sarma, G.B., Dawson, P.R., 1996. Texture predictions using a polycrystal plasticity model incorporating neighbor interactions. Int. J. Plasticity 12, 1023.

Underwood E.E., 1970. Quantitative Stereology. Addison-Wesley Publishing Co., Reading, MA.

Wanheim, T., Bay, N., 1978. A model for friction in metal forming processes. Annals of the CIRP 27, 189-194.

Wert, J.A., Huang, X., Winther, G., Pantleon, W., Poulsen H.F., 2007. Revealing deformation microstructures. Materialstoday 10, 24-32.

Zhang X., 2009. Quantitative investigation of microstructural evolution during the cold wire-drawing of a pearlitic steel wire and its relationship with mechanical properties. Tinghua University, Beijing, China.

Zhang, X., Godfrey, A., Liu, W., Liu, Q., 2011. Study on dislocation slips in ferrite and deformation of cementite in cold drawn pearlitic steel wires from medium to high strain. Mater. Sci. Technol. 27, 562-567.

Zhang, X., Hansen, N., Gao, Y., Huang, X., 2012a. Hall–Petch and dislocation strengthening in

graded nanostructured steel. Acta Mater. 60, 5933-5943.

Zhang, X., Godfrey, A., Winther, G., Hansen, N., Huang, X., 2012b. Plastic deformation of submicron-sized crystals studied by in-situ Kikuchi diffraction and dislocation imaging. Materials Characterization 70, 21-27.

Zhang, X., Hansen, N., Godfrey, A., Huang, X., 2018. Structure and strength of sub-100 nm lamellar structures in cold-drawn pearlitic steel wire. Materials Science and Technology 34, 794-808.

Zhu, K.N., Godfrey, A., Hansen, N., Zhang X.D., 2017. Microstructure and mechanical strength of near-and sub-micrometre grain size copper prepared by spark plasma sintering. Materials & Design 117, 95-103.

Highlights

- For compressed cylinders the macroscopic stress and strain relate to the boundary spacing D_{av} and the boundary area per unit volume $S_v = 2/D_{av}$ where D_{av} is the average spacing between deformation induced low angle boundaries and high angle boundaries (>15°) indistinguishable from grain boundaries. The flow stress can be expressed by a Hall-Petch formulation where the strength contribution from all boundaries is $k_2 {D_{av}}^{-0.5}$ where k_2 is a constant and $1/D_{av}$ depends on the equivalent strain as expressed in a bilinear relationship.
- The compressed rings showed large variations in stress, strain and microstructure when characterized by three complementary techniques: microhardness testing, electron microscopy (EBSD) and FEM. Results for 14 areas (50×50 μm^2) in two rings follow the same trend with good agreement between the local stress and strain when calculated based on D_{av} quantified by EBSD or simulated by a FEM analysis.
- The comparison of the microstructural analysis and the simulation shows the strength of using complementary characterization techniques when analyzing a heterogeneous structure with structural variations covering multiple length scales. The comparison also supports the hypothesis that the microstructure in local regions of a heterogeneous structure evolves in accordance with universal principles established for homogeneously deformed polycrystalline metals.